

## Many routes to turbulent convection

By J. P. GOLLUB AND S. V. BENSON†

Physics Department, Haverford College, Haverford, Pa 19041, U.S.A.

(Received 25 September 1979)

Using automated laser-Doppler methods we have identified four distinct sequences of instabilities leading to turbulent convection at low Prandtl number ( $2.5$ – $5.0$ ), in fluid layers of small horizontal extent. Contour maps of the structure of the time-averaged velocity field, in conjunction with high-resolution power spectral analysis, demonstrate that several mean flows are stable over a wide range in the Rayleigh number  $R$ , and that the sequence of time-dependent instabilities depends on the mean flow. A number of routes to non-periodic motion have been identified by varying the geometrical aspect ratio, Prandtl number, and mean flow. Quasi-periodic motion at two frequencies leads to phase locking or entrainment, as identified by a step in a graph of the ratio of the two frequencies. The onset of non-periodicity in this case is associated with the loss of entrainment as  $R$  is increased. Another route to turbulence involves successive subharmonic (or period doubling) bifurcations of a periodic flow. A third route contains a well-defined regime with three generally incommensurate frequencies and no broadband noise. The spectral analysis used to demonstrate the presence of three frequencies has a precision of about one part in  $10^4$  to  $10^5$ . Finally, we observe a process of intermittent non-periodicity first identified by Libchaber & Maurer at lower Prandtl number. In this case the fluid alternates between quasi-periodic and non-periodic states over a finite range in  $R$ . Several of these processes are also manifested by rather simple mathematical models, but the complicated dependence on geometrical parameters, Prandtl number, and mean flow structure has not been explained.

---

### 1. Introduction

The behaviour of a thin fluid layer heated from below has been of great importance in the development and gradually increasing sophistication of nonlinear hydrodynamics. The Rayleigh–Bénard instability is well understood, and convecting solutions of the nonlinear hydrodynamic equations have been found for layers of infinite horizontal extent. The linear stability of this flow with respect to various disturbances has been examined, and various secondary instabilities predicted and observed (Busse 1980). Some of these secondary instabilities change the spatial structure of the velocity field without the addition of time dependence, while others result in an oscillatory flow. However, more complex time-dependent flows and the onset of turbulence have remained out of reach theoretically.

Oscillatory instabilities have been observed experimentally, but secondary instabilities leading to quasi-periodic flows with several distinct frequencies have not been

† Present address: Physics Department, Stanford University, Stanford, Ca 94305.

identified. Furthermore, such flows cannot be easily distinguished from turbulent flows by qualitative observations. Many elementary questions have not yet been answered. How many instabilities occur as the temperature gradient across a fluid layer is increased? What is the nature of the time-dependent flows that occur? Is there a well-defined temperature gradient at which non-periodic flow begins? How does the sequence of instabilities depend on the parameters of the system?

The experiments reported in this paper utilize significant innovations in order to address these questions. A non-perturbative laser-Doppler probe with computer control and data acquisition allows the space and time structure of the velocity field to be examined in great detail. The statistical properties of the flow are determined by power spectral analysis capable of detecting secondary flows far too weak to observe visually. Precision control of the thermal environment allows external perturbations to be largely eliminated, and changes in the dynamical behaviour resulting from small parameter increments to be detected. Using these methods, we are able to distinguish clearly between periodic, quasi-periodic, and non-periodic flows. By varying the geometry and Prandtl number, we have observed instabilities leading to quasi-periodic flows with two and three independent frequencies; phase-locking phenomena involving these various frequencies; subharmonic or period-doubling bifurcation of periodic convective flows; and intermittent non-periodicity. At least four qualitatively different sequences of instabilities can lead to turbulence in this system.

The paper is organized in the following fashion. In §2 we review previous theoretical and experimental work on the transition to turbulent convection. Section 3 contains a description of the fluid system, the laser-Doppler technique, signal processing electronics, and the methods used to compute spectra and contour maps. Our results for the various routes to turbulent flow are presented in §4, and discussed in the light of other experiments and theoretical models in §5.

## 2. Background

The flow of a fluid confined to a horizontal layer and heated from below is defined by a small number of parameters. We denote the separation between highly conducting parallel plates by  $d$ , and the temperature difference between them by  $\Delta T$ . The state of the fluid depends on the boundary conditions and two dimensionless parameters, the Rayleigh number  $R = g\alpha d^3 \Delta T / \kappa \nu$ , and the Prandtl number  $P = \nu / \kappa$ , where  $\nu$  is the kinematic viscosity of the fluid,  $\alpha$  is the thermal expansion coefficient,  $\kappa$  is the thermal diffusivity, and  $g$  is the gravitational acceleration. This paper is concerned with the range  $2 \leq P \leq 5$ . It is often convenient to use the relative Rayleigh number  $R/R_c = \Delta T / \Delta T_c$ , where  $\Delta T_c$  is the temperature difference at which convection begins in an infinite layer. For a fluid layer of finite horizontal extent, a third important parameter is the aspect ratio  $\Gamma$ , defined for rectangular boundaries as the ratio of the largest horizontal dimension to the layer thickness.†

### 2.1. Time-independent convection

The form of the time-independent convection that precedes the onset of time dependence is discussed by Busse (1978, 1980), Koschmieder (1974), Normand, Pomeau & Velarde (1977) and Dubois & Bergé (1978). Of particular relevance is the fact that, in

† One can also define a *horizontal* aspect ratio as the ratio of the two horizontal dimensions.

a rectangular parallelepiped of small aspect ratio, both calculations (Davis 1967) and experiments (Stork & Müller 1972) show that convection near its onset usually has the form of rolls oriented parallel to the short side of the cell. The onset is delayed somewhat beyond the value  $R_c$  which characterizes an infinite fluid layer. Furthermore, the flows are not generally unique. Several different flows have been observed experimentally to be stable for a given geometry, Rayleigh number and Prandtl number. For example, the number of rolls may vary (i.e. the dominant wave-number may have several different values). Any given flow pattern is stable over a wide range in  $R$  if the aspect ratio is small. Because of this non-uniqueness, which is incompletely understood theoretically, it is important to supplement local measurements of time-dependent phenomena with a method capable of yielding the overall spatial structure of the flow. In practice, we found that the multiplicity of stable states was substantially greater than calculations and previous experiments suggest.

### *2.2. The onset of time dependence*

A stability theory for the onset of time dependence was presented by Clever & Busse (1974) and Busse & Clever (1978), who superimposed infinitesimal disturbances on the parallel convection rolls for a layer of infinite extent. Whereas the onset of convection is independent of  $P$ , the onset of time dependence is strongly dependent on  $P$ . For large  $P$ , secondary instabilities involving complex three-dimensional stationary structures precede the onset of time dependence. However, for sufficiently low  $P$ , Clever & Busse predicted that the onset of time dependence would be a transverse oscillation of the basic convective rolls. This instability was observed by Willis & Deardorff (1970), Krishnamurti (1970, 1973), and Ahlers & Behringer (1979). Even when a transition to three-dimensional convection precedes the onset of time dependence, the oscillatory instability seems to be qualitatively similar to the predictions for low  $P$  (Busse & Whitehead 1974).

### *2.3. Transition to turbulent convection*

The possible existence of further time-dependent instabilities has not been investigated by stability analysis because of mathematical complexity. However, there have been several numerical studies based on highly truncated normal mode expansions. The first of these is the well-known study by Lorenz (1963) of a model originally due to Saltzman (1962). The model assumes a two-dimensional flow and contains only three time-dependent amplitudes from the expansions of the velocity and temperature fields. Numerical integration of the equations shows non-periodic behaviour for certain parameter values even though there are only three degrees of freedom.

Curry (1978) has recently generalized Lorenz' model by retaining additional variables for a total of 14 time-dependent amplitudes. This model is still not realistic because of its two-dimensionality and lack of lateral boundaries. Nevertheless, it manifests a much greater variety of phenomena: a bifurcation to a limit cycle or periodic oscillation, a subharmonic bifurcation in which the dominant oscillation frequency is halved, an instability leading to quasi-periodic motion with two distinct frequencies, and non-periodic motion.

McLaughlin & Martin (1975) have extended the idea of Lorenz in a way that dispenses with the unrealistic requirement of two-dimensionality. This model of 39 coupled variables shows both periodic and chaotic states for reasonable values of the

parameters of the problem. The calculations were not extensive enough to provide evidence for quasi-periodic flows.

Lipps (1976) simulated stationary and time-dependent convection at  $P = 0.7$  using the full hydrodynamic equations in the Boussinesq approximation (Busse 1978). Periodic boundary conditions at lateral boundaries were assumed, along with perfectly conducting vertical boundaries. Examples of both periodic and apparently non-periodic convection were found, but the numerical solutions did not extend to large enough times to permit reliable discrimination between periodic and non-periodic flows to be made.

Overall, the theoretical picture of the transition to turbulent convection is quite muddy. It is not known what occurs beyond the onset of oscillations, and how the phenomena depend on  $P$  and the aspect ratio.

Recently Ahlers (1974) and Ahlers & Behringer (1978, 1979) have used precision thermal methods at cryogenic temperatures to study the heat transport in convecting liquid helium with cylindrical lateral boundaries. They observed a striking dependence of the qualitative behaviour on the aspect ratio (the ratio of radius to depth). For small aspect ratio, distinct periodic and quasi-periodic regimes precede the onset of non-periodic motion. However, for large aspect ratio non-periodic motion begins very near  $R$  with no intervening periodic regimes. Some aspect ratio dependence has also been found by Libchaber & Maurer (1978) using a local temperature probe.

The present study employs somewhat higher Prandtl numbers (2.5 and 5.0), rectangular cells of relatively small aspect ratio and a laser-Doppler probe for both local measurements and flow mapping. Some preliminary results of our work were reported in Gollub *et al.* (1977), Fenstermacher, Swinney, Benson & Gollub (1979) and Gollub & Benson (1978, 1979).

### 3. Experimental techniques

#### 3.1. Convection cell

In order to permit a range of Prandtl numbers to be investigated in a single system, we selected water as the working fluid. The strong temperature dependence of the viscosity of water allows  $P$  to be varied between 9 and 2 by varying the mean working temperature between 10 and 90 °C. High Rayleigh numbers can be reached with a relatively thin cell, a fact that permits the entire system to be small and thermally stable. However, the Oberbeck-Boussinesq approximation (Busse 1978) was not particularly well satisfied. The viscosity (or locally defined Prandtl number) varied by  $\pm 10\%$  over the fluid layer under the most extreme conditions we employed; more typically the variation was  $\pm 2\%$ .

The cell was designed with an emphasis on temperature stability and horizontal temperature uniformity, because external perturbations can obscure the onset of intrinsic dynamical noise in the fluid, and non-uniformities can blur sharp transitions. The system design is shown in figure 1. Two copper plates of horizontal dimensions 9.3 by 6.7 cm and thickness 2.54 cm (upper) and 1.27 cm (lower), are separated by a Plexiglas spacer of variable interior size containing the fluid. The space around the cell is evacuated in order to eliminate convective heat loss from the sides of the cell, and the surrounding vacuum can is kept at the mean working temperature to minimize radiative heat loss. The temperature gradient at the lateral fluid boundary cannot be

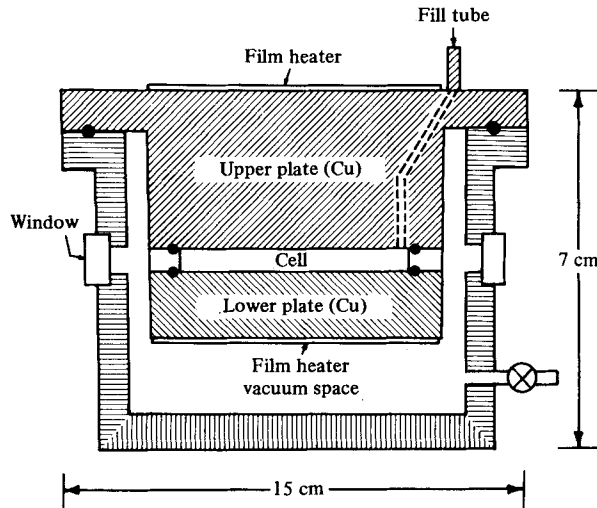


FIGURE 1. Schematic diagram of convection cell showing vacuum space and optical access.

assumed to be uniform, although good thermal contact between the copper and Plexiglas was maintained by silicone grease.

Results for two aspect ratios are reported in this paper. The first cell has interior dimensions 16.42 by 27.72 by 7.90 mm high (aspect ratio  $\Gamma = 3.51$ ) and the second is 14.66 by 28.85 by 11.94 mm high ( $\Gamma = 2.42$ ). Some preliminary observations on a larger rectangular cell ( $\Gamma = 10.0$ ) and a circular cell (radius to height ratio of 3.14) were previously reported (Gollub *et al.* 1977; Fenstermacher, Swinney, Benson & Gollub 1979).

The temperatures of the two copper plates are controlled by a.c. bridges using sensitive thermistors and lock-in amplifiers. The d.c. output of each lock-in drives a resistive film heater via an operational power supply. There are three feedback loops altogether: two a.c. bridges for the copper plates, and a commercial d.c. bridge controller for the vacuum can and heat shield. Temperatures were measured using four additional matched and calibrated thermistors embedded in the copper near the fluid.

The long term (4 h) thermal stability of this system is within about 1–2 mK, corresponding to effective fluctuations in  $\Delta T$  of about 0.05%. (At  $R/R_c = 25$ ,  $\Delta T$  was typically several k.) It is difficult to do much better than this in a system that cannot be completely isolated owing to the necessary heat flux through it. The readings of the different thermistors on each plate indicate a horizontal temperature uniformity of better than 0.5% of  $\Delta T$ .

### 3.2. Laser-Doppler velocimetry (LDV)

A dual beam forward scatter LDV system is used for both flow mapping and local velocity measurements in real time. The optical arrangement is shown in figure 2(a). A vertically polarized 15 mW laser beam at 6328 Å is first split into two beams of equal intensity, and then each part is frequency shifted by scattering from an acoustic wave in a liquid. Each beam is shifted by about 40 MHz, but the frequency difference between the two shifts is accurately maintained at 2000.0 Hz by electronic feedback techniques. The two shifted beams are then focused by a lens of focal length 12 cm to a point inside the convecting fluid, which is doped with polystyrene latex spheres of

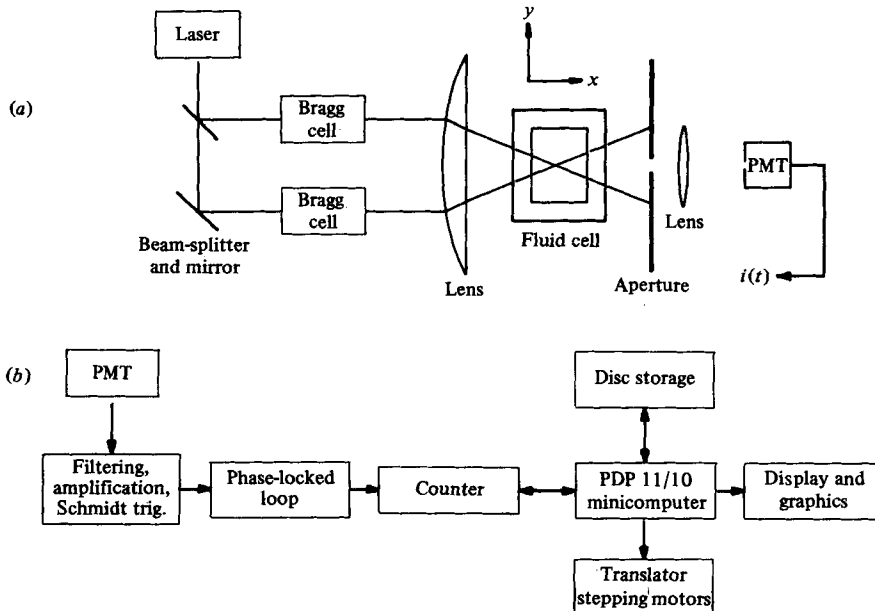


FIGURE 2. Schematic diagrams of (a) laser-Doppler optics, and (b) signal-processing electronics and data-acquisition system. The photocurrent  $i(t)$  in (a) oscillates at a frequency proportional to the fluid velocity component  $V_y$ .

diameter  $0.369 \mu\text{m}$ . The scattering volume is the ellipsoidal region of intersection of the two beams, and has major ( $x$ ) and minor ( $y$ ) axes of about  $500 \mu\text{m}$  and  $60 \mu\text{m}$  respectively. Since the beam profiles are actually gaussian, the boundaries of the scattering volume are not precisely defined. Scattered light from a small solid angle of about  $5 \times 10^{-5}$  sr is collected by a lens and focused on a  $200 \mu\text{m}$  pinhole in front of a photomultiplier.

The optical system is sensitive to the velocity component  $V_y(\mathbf{r}, t)$  in the  $y$  direction in figure 2. Light scattered from one beam by particles moving in this direction is advanced in phase, while light scattered from the other beam is retarded in phase. Since the photocurrent is proportional to the square of the optical field, it contains a component oscillating at the difference frequency of the light scattered by the two beams:

$$\nu = 2000 \text{ Hz} + V_y n \lambda_0^{-1} \sin(\frac{1}{2}\theta),$$

where  $\lambda_0$  is the vacuum wavelength,  $n$  is the index of refraction of the water, and  $\theta = 13.6^\circ$  is the angle between the two beams. The acoustic frequency shifters permit velocities of stationary or slow particles to be measured easily. The velocity component measured is horizontal and generally perpendicular to the axes of the convective rolls. The optical system is non-perturbative since very little of the light is absorbed by the fluid.

### 3.3. Data acquisition

The photomultiplier signal is amplified and bandpass filtered to remove most of the high-frequency shot noise and the low-frequency amplitude fluctuations. A Schmidt trigger then precedes the input to a phase-locked loop, which locks the frequency of an external voltage-controlled oscillator (VCO) to the Doppler frequency, with some

reduction in the bandwidth of the frequency fluctuations and consequent noise reduction. Finally, the VCO frequency is determined by counting cycles over a time interval of 0.5–2 s with a commercial counter controlled by a Digital Equipment Corporation PDP 11/10 minicomputer.

The minicomputer is used for experimental control, data acquisition, and analysis in two distinct modes. The fluid system is mounted on computer-controlled stepping-motor-driven translation stages with a resolution of about 0.005 mm for motion in either the  $x$  or  $y$  direction. Contour maps of the velocity field are obtained by measuring  $V_y$  at each point in a rectangular grid of up to 450 points in a horizontal plane. Software is used both to perform the sampling and to plot contour maps of constant Doppler shift using linear interpolation between points. About 60 min are required to acquire the data to construct a contour map if the velocity field is time independent. If the field is oscillating in a periodic state, the velocity is averaged over one cycle at each grid point in order to yield a map of the mean velocity. If the fluid motion is non-periodic, mean velocity contour maps are less precise unless very long averaging times are used to eliminate fluctuations due to low-frequency noise in the fluid.

The second mode of data acquisition involves measuring the time-dependent velocity at a single location. Sampling times  $\Delta t$  are long enough (0.5–2 s) to obtain accurate measurements of the Doppler frequency, which is in the range 1500–2500 Hz, but much shorter than the characteristic frequencies of the fluid motion. The accuracy of the timing routines was found to be better than  $10^{-5}$  s, and fluctuations in timing are less than this. Typical runs consist of  $N = 4096$  sequential data points. Longer runs require an inordinate amount of time without yielding much more information.

Velocity power spectra are computed from the squared modulus of the fast Fourier transform of the sampled velocity. We use a Cooley–Tukey FFT algorithm, and apply a GEO window (Otnes & Enochson 1972) to suppress side lobes caused by the finite duration  $T = N\Delta t$  of the record. Spectral estimates are obtained at frequency intervals of  $1/T = 1/N\Delta t$  up to the Nyquist frequency  $f_N = (2\Delta t)^{-1}$ . The methods used to minimize aliasing are discussed by Fenstermacher, Swinney & Gollub (1979).

The resolution of the computed spectra is approximately equal to the interval  $1/T$  between spectral estimates. Often, the spectra show peaks with approximately this resolution. If one assumes that they are actually discrete spectral lines, their frequencies can be computed to an accuracy much better than  $1/T$ . A power-weighted average of the frequencies of the two largest spectral estimates within a peak can be used to extract this information, and is accurate to about 5% of  $1/T$ . The deviations are a systematic function of the frequency of the peak and the frequencies at which the spectral estimates are computed, a function which we obtained from artificial data of known frequency. By employing this correction to the power-weighted average, we are able to obtain discrete frequencies to an accuracy of about 1% of  $1/T$  ( $10^{-5}f_N$ ) if there is little noise. We tested our procedure for computing spectral peaks on artificial data with and without background noise. The standard deviation  $\sigma_f$  of the frequency determination was found to depend on the ratio  $A_n/A_p$  of the integrated noise (up to  $f_N$ ) to the area under the peak, as shown in figure 3. The precision of frequency determination is degraded when the peak height is not far above the background noise level.

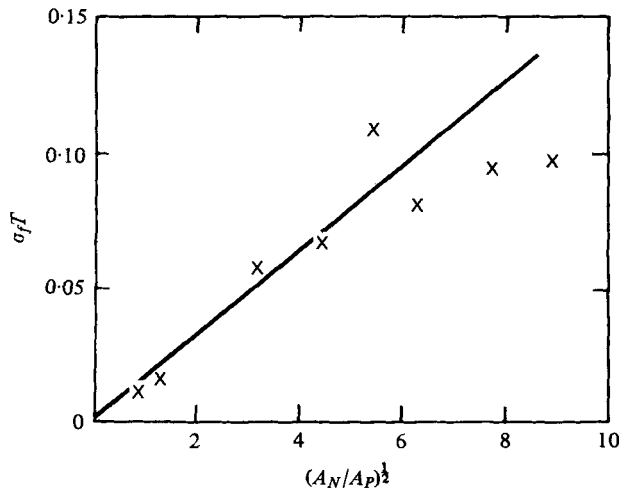


FIGURE 3. Standard error  $\sigma_f$  (in units of the spacing  $T^{-1}$  between spectral estimates) for frequency determination, as a function of the ratio  $A_N/A_P$  of the integrated area of the background noise to that of the peak. The crosses were obtained from empirical tests on artificial data having a single known frequency and broadband noise. The line is the estimated standard error actually used in analysing data. As an example, a peak 2 orders of magnitude above the noise typically yields  $A_N/A_P = 10$  so  $\sigma_f = 0.05/T$  in this case.

## 4. Experimental results

### 4.1. Mean flow patterns

Although the main purpose of this work was to study the time-dependent regimes, the non-uniqueness of spatial states (§ 2.1) made it necessary to monitor the mean flow using the contour mapping technique of § 3.3. Several distinct mean flows were found to be stable in each of the convection cells, and examples are shown in figure 4. Contours of constant Doppler shift represent the velocity component parallel to the  $y$  axis (figure 2*a*), in a horizontal plane above the centre of the cell. The geometry is such that the rolls generally align parallel to  $x$ , which is the short cell dimension. Positive and negative shifts correspond to motion in the positive and negative  $y$  directions, respectively. In the flow of figure 4(*a*) fluid rises (out of the page) in the centre of the cell, moves toward the edges and descends. The line of zero shift (dashed) marks the vertical boundary between convective rolls. The contour line labelled 400 Hz corresponds to a velocity component of  $0.082 \text{ cm s}^{-1}$ . (The lines do not extend to the edges of the cell because optical distortions reduce the accuracy of measurement there.) These contour maps are reproducible after a day with very little change.

In both of the cells that were studied in detail, the most stable mean flow (figure 4*a*) can be qualitatively summarized as two symmetrical rolls oriented with axes parallel to the short side of the cell. For  $\Gamma = 3.5$  it is stable over the entire range of Rayleigh number studied ( $2 < R/R_c < 100$ ). For  $\Gamma = 2.4$  this flow is stable up to  $R/R_c = 85$  when  $P = 5$ , and stable up to  $R/R_c = 110$  when  $P = 2.5$ . The velocity field is approximately two-dimensional away from the ends of the rolls. The variation of  $V_y$  with  $y$  (figure 5*a*) is a distorted sinusoid with harmonics that become relatively more prominent as  $R$  is increased. However, even at  $R/R_c = 17.7$ , only the first four terms of the Fourier expansion for  $V_y(y)$  are significant, as shown in figure 5(*b*). This observation

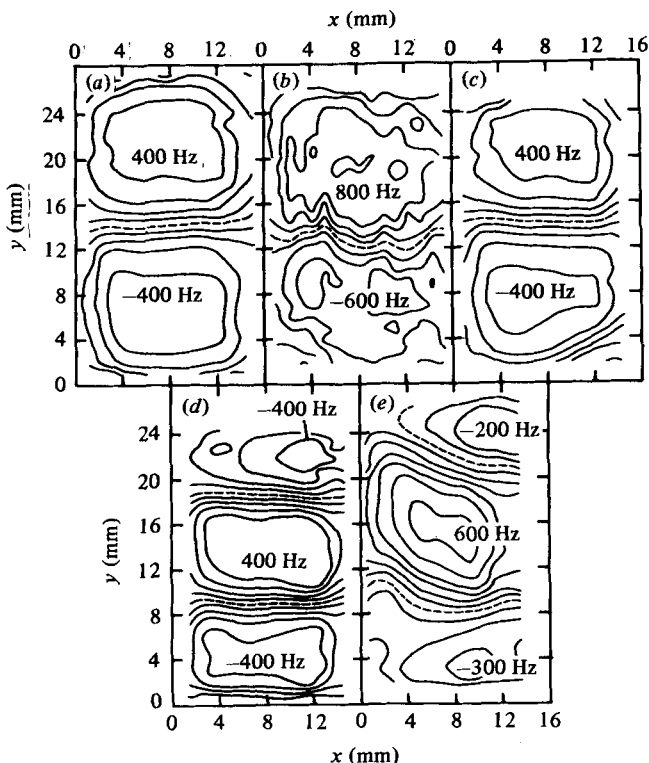


FIGURE 4. Contour maps of constant Doppler shift for the mean velocity component  $\bar{V}_y$ , measured in a horizontal plane slightly above the centre of the convection cell (see text). (a) Two symmetrical rolls ( $P = 2.5$ ,  $\Gamma = 3.5$ ,  $R/R_c = 17.1$ ); (b) two rolls persist in the mean flow, although the fluid is strongly non-periodic ( $P = 5.0$ ,  $\Gamma = 3.5$ ,  $R/R_c = 65.4$ ); (c) a distorted but stable two-roll flow ( $P = 2.5$ ,  $\Gamma = 3.5$ ,  $R/R_c = 18.1$ ); (d) three rolls ( $P = 5.0$ ,  $\Gamma = 3.5$ ,  $R/R_c = 30.9$ ); (e) a complex mean flow for a periodic state in which the rolls are also inclined to the vertical ( $P = 5.0$ ,  $\Gamma = 2.4$ ,  $R/R_c = 84.7$ ).

indicates that a truncated normal-mode expansion would probably not require an inordinate number of terms to represent even the full three-dimensional velocity field.† Even at  $R/R_c = 84.7$ , where the flow is chaotic, the contour map of figure 4(b) shows that the two-roll flow persists in a time-averaged sense. Some of the irregularities in this figure may be artifacts of the finite averaging time (8 s) at each grid point. Further detailed study of these maps is intended.

Other mean flows that are also stable over a wide range in  $R$  can be obtained from different initial conditions. For example, cooling the upper plate rather than heating the lower one to attain the desired Rayleigh number yields a mean flow almost identical to figure 4(a) but with signs reversed, indicating that the fluid descends at the centre of the cell and rises at the edges.

Somewhat surprising is the observation of stable mean flows differing in relatively small but still significant ways from the basic two-roll flow. By stability, we mean that a flow persists without noticeable change for a time long compared to the horizontal

† The functional form of the velocity field in time-independent convection has recently been studied by Dubois & Bergé (1978). The amplitudes of the first few spatial Fourier components were found to be in good agreement with theoretical predictions for  $R/R_c < 10$ .

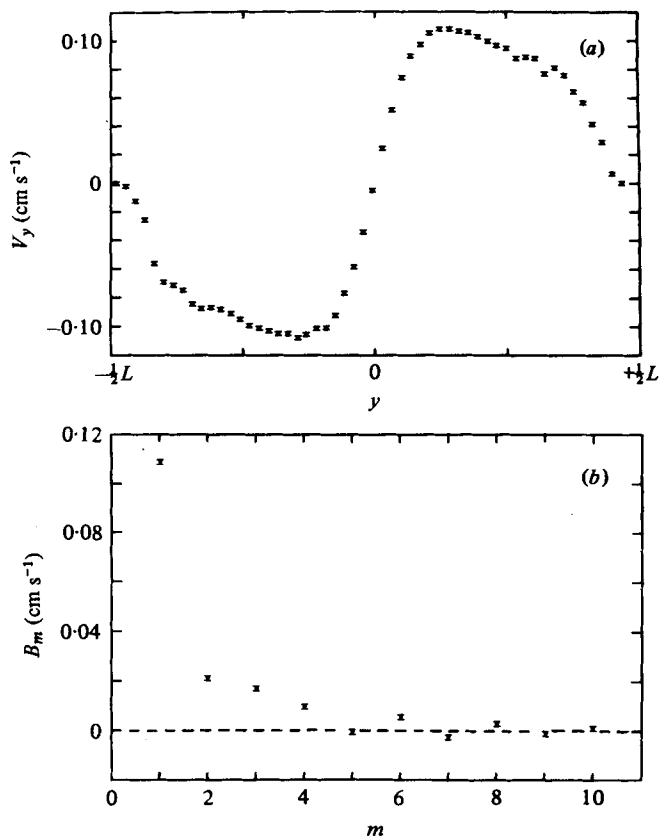


FIGURE 5. (a) Fluid velocity component  $V_y$  as a function of  $y$  for the flow of figure 4(a). (b) Fourier coefficients  $B_m$  of the curve in (a). Only the first four terms are significant.  $R/R_c = 17.7$ .

thermal diffusion time, which is about  $10^4$  s for our cells. In this sense, the flow of figure 4(c), in which one roll appears distorted, is stable at least over the range  $18 < R/R_c < 40$  (at  $\Gamma = 3.5$ ). This flow evolves into a sequence of time-dependent states substantially different from those associated with figure 4(a).

A mean flow with three rolls was observed in the larger cell ( $\Gamma = 3.5$ ), and its contour map appears in figure 4(d). It loses stability with respect to the two-roll flow when  $R/R_c$  exceeds a threshold somewhat above 50 at  $P = 5$ .

In the cell with smaller aspect ratio ( $\Gamma = 2.4$ ) yet another distinct mean flow was observed in which the two rolls become highly inclined to the vertical, and an eddy forms in a corner. This behaviour is shown in figure 4(e), and occurs for  $R/R_c > 85$  at  $P = 5$ . It can also appear with signs reversed.

Other mean flows can be obtained in these cells in addition to the ones we have discussed, but they are not stable over a large range in  $R$ . Because of the multiplicity of spatial states, we adopted the following procedure for studying time-dependent phenomena. After selecting the aspect ratio and Prandtl number, one of the stable mean flows was chosen by manipulation of the boundary temperatures, and verified by taking a contour map. Then the time dependence was studied at a single location in the cell by spectral analysis. The Rayleigh number was increased and then decreased in

small steps, with occasional verification that the mean flow structure had not changed. Several weeks of data taking were required to complete such a sequence.

#### 4.2. Transition to turbulence

We have observed several qualitatively different types of time-dependent flow. It will be useful in describing them to introduce a simple set of abbreviations. Periodic time dependence (P) evolves from a stationary flow (S) and is recognized by a velocity power spectrum containing a single instrumentally sharp peak and perhaps harmonics, but no broadband noise, except for instrumental noise. It is possible for a periodic motion to undergo a subharmonic bifurcation to another periodic state ( $P_2$ ) or ( $P_4$ ) in which the fundamental frequency is half or one quarter of the original frequency. Quasi-periodic states ( $QP_2$ ) and ( $QP_3$ ) are recognized by spectra containing respectively two or three incommensurate frequencies, along with sums and differences of these frequencies, but no broadband noise. The two frequencies in a state  $QP_2$  can lock to a rational ratio. The resulting flow, denoted (L), is actually periodic. If the velocity spectrum contains any broadband noise, the motion is non-periodic (N) even if relatively sharp spectral peaks are also present. We regard non-periodic motion as being weakly turbulent. However, some workers reserve the latter term for flows that are known to vary randomly in space as well as time (Monin 1979).

The sequence of instabilities leading to non-periodic flow depends on the aspect ratio, Prandtl number, and mean flow. The major sequences we have observed are summarized by the bar graphs in figure 6. Each graph is labelled by a Roman numeral specifying a route to non-periodicity described in the following sections, and by a letter denoting one of the mean flows of figure 4.

#### 4.3. Route I: quasi-periodicity and phase locking

Non-periodicity preceded by quasi-periodicity and phase locking is observed under several different conditions, as shown in figure 6. The basic path is specified by the symbolic sequence  $P \rightarrow QP_2 \rightarrow L \rightarrow N$ . We describe the observations in detail for the case  $\Gamma = 3.5$  and  $P = 5.0$ . The mean flow is that of figure 4(a) throughout the time-dependent regimes studied.

A sequence of velocity records and corresponding power spectra for increasing  $R$  is shown in figure 7. The duration of each velocity record is 6144 s, only a small portion of which is shown. Power spectra are plotted on a logarithmic vertical scale. The instrumental background noise is that of figure 7(a) and corresponds to a root mean square noise in the Doppler shifts of only 2 Hz. The spectral peaks are instrumentally sharp even when the duration of the run is doubled, and the strongest peak is four orders of magnitude above the instrumental noise. The integrated noise to peak ratio  $A_n/A_p$  defined in § 3.3 is 0.1, and figure 3 then implies that the frequencies of the peaks can be determined to an accuracy of  $0.01T^{-1} = 10^{-6}$  Hz. However, peaks in the plotted spectra are broadened because four adjacent spectral estimates have been averaged in order to reduce the background fluctuations. The observed sequence of instabilities is as follows:

1. A bifurcation leads to a transfer of stability from time-independent flow to periodic flow at  $R/R_c = 27.2$ . This instability (like the others described in this section) has a hysteresis of about  $\pm 0.15R_c$  depending on the direction in which  $R$  is changed. The frequency labelled  $f_2$  (for historical reasons) in figure 7(a) appears at all points in

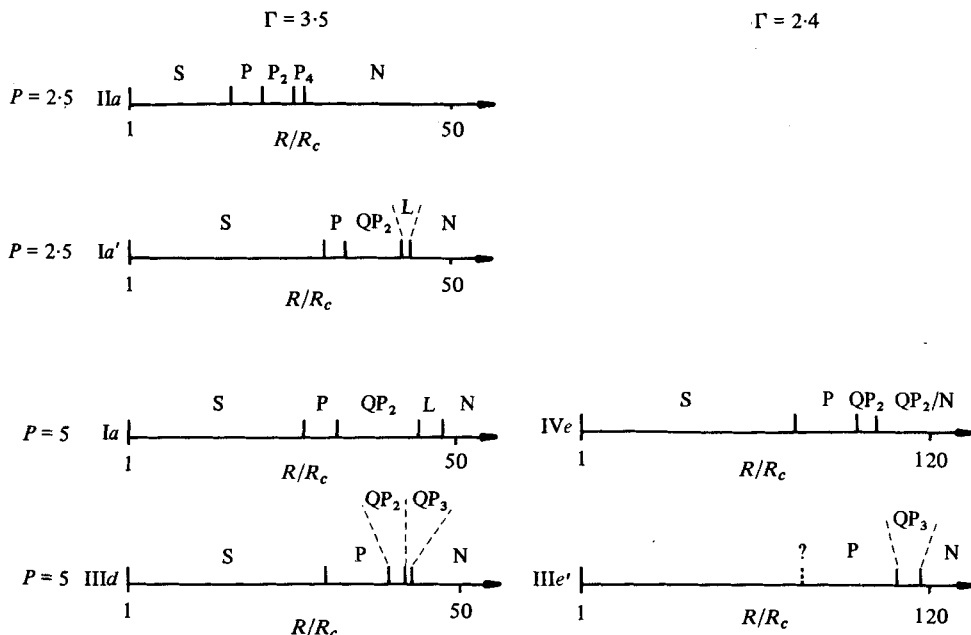


FIGURE 6. Bar graphs of the various instabilities leading to non-periodicity as a function of the aspect ratio  $\Gamma$ , the Prandtl number  $P$ , and the mean flow pattern. Roman numerals denote the routes to non-periodicity we have identified, and are keyed to the subheadings of §4. The lower-case letters refer to the mean flows of figure 4, except that a prime indicates sign reversal.

the cell, along with harmonics at integral multiples of the fundamental. The amplitudes of the fundamental and harmonics vary with position in the cell, but the frequencies are invariant.

2. At  $R/R_c = 32$  a second frequency appears in the spectrum (throughout the cell), as shown in figure 7(b). All of the peaks have been identified, to within the estimated standard error  $\sigma_f$ , as linear combinations of two basic frequencies of the form

$$f = m_1 f_1 + m_2 f_2,$$

where  $m_1$  and  $m_2$  are integers,  $f_1 = 0.03082$  Hz and  $f_2 = 0.08348$  Hz. The presence of high-order mixing components in the spectrum indicates that these time-dependent processes are strongly nonlinear. The ratio  $f_2/f_1$  decreases smoothly with increasing Rayleigh number, suggesting that the two frequencies are at least sometimes incommensurate and hence that the spectrum corresponds to a quasi-periodic motion.†

3. Phase locking of the two frequencies occurs when  $R/R_c$  exceeds 44.4. This can be seen as a step in the ratio  $f_2/f_1$ , as shown in figure 8. The ratio decreases smoothly until the step is reached, where  $f_2/f_1 = 2.333 \pm 0.001 = \frac{7}{3}$ . It is interesting to note that the locking ratio is not exactly reproducible from experiment to experiment. The cause of this is unknown. A spectrum corresponding to locking at the ratio  $\frac{9}{4}$  is shown in figure 7(c). Because of the locking, the spectrum corresponds to periodic motion at a

† There is some ambiguity in the choice of the second frequency  $f_1$  because it is not the strongest line at all locations in the cell. One could choose the peak at 0.11430 Hz instead as  $f_1$ , but this change would not have any important effect.

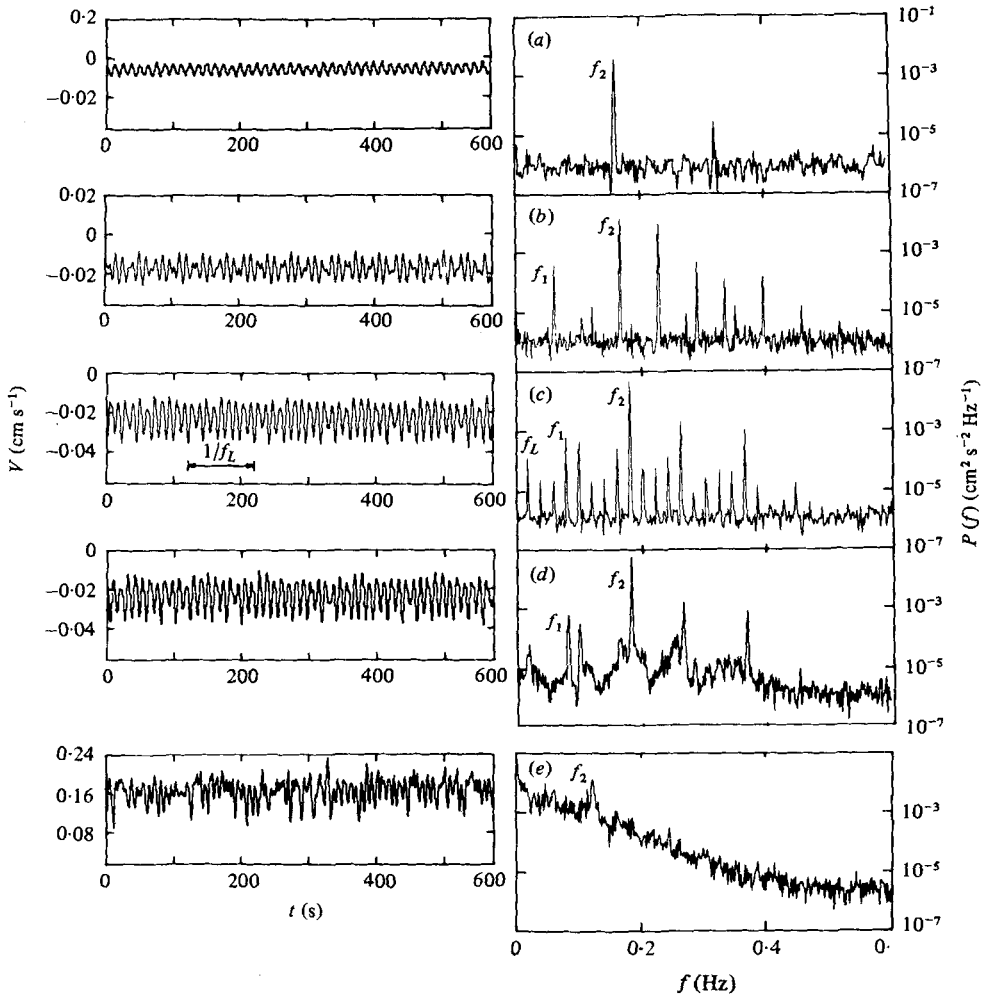


FIGURE 7. Velocity records and power spectra showing the sequence of instabilities leading to non-periodic flow (route Ia). The sequence consists of: (a) a periodic state with a single peak and its harmonics,  $R/R_c = 31.0$ ; (b) a quasi-periodic state with two incommensurate frequencies  $f_1$  and  $f_2$  and many of their linear combinations,  $R/R_c = 35.0$ ; (c) phase locking at the integer ratio  $f_2/f_1 = \frac{2}{3}$ ,  $R/R_c = 45.2$ ; (d) a non-periodic state with relatively sharp peaks just above the onset of noise,  $R/R_c = 46.8$ ; and (e) a strongly non-periodic state with no sharp peaks showing the broadband noise far above its onset,  $R/R_c = 65.4$ .

frequency  $f_L = \frac{1}{3}f_2 = \frac{1}{4}f_1$ . Strong mixing induced by the locking creates strong peaks at all multiples of  $f_L$ . No locking has been observed at lower  $R$ , suggesting that the strength of the nonlinear interaction between the two oscillations is weaker there.

4. The spectra develop broadband noise and the peaks begin to broaden at  $R/R_c = 46.0$ , indicating the onset of non-periodic motion. At the same Rayleigh number, to within experimental error, the ratio  $f_2/f_1$  starts to decrease again. Thus, the onset of non-periodicity coincides with the loss of entrainment of the two oscillations. The ratio of the two frequencies is not measurable with high accuracy beyond  $R/R_c = 46.5$ ,

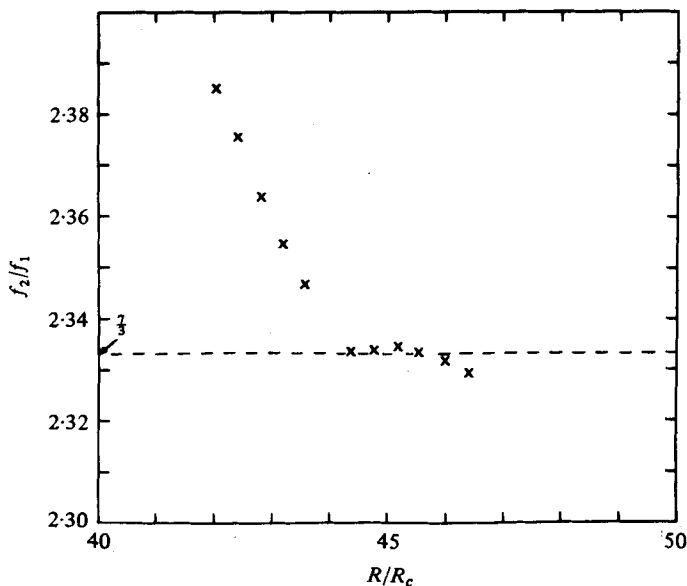


FIGURE 8. Frequency ratio  $f_2/f_1$  plotted as a function of  $R$  for route Ia. The ratio has a step indicating phase locking in the range  $44.4 < R/R_c < 46.0$ . The errors in the values are approximately equal to the size of the symbols.

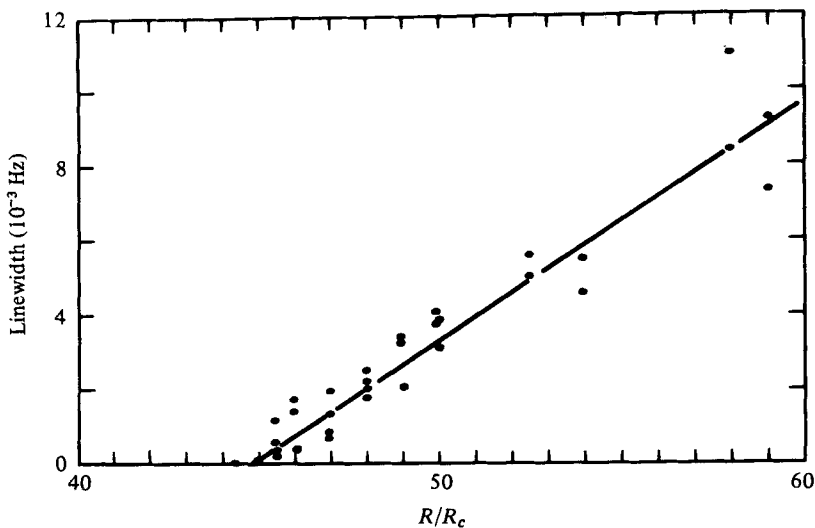


FIGURE 9. Linewidth of the spectral peaks beyond the onset of noise, with the instrumental linewidth subtracted. The variation is linear in  $R/R_c$  above the threshold.

so the data in figure 8 end at this point. The spectrum in figure 7(d) shows the broadband noise near its onset, where relatively sharp (but not instrumentally sharp) peaks still exist, but the high-order mixing peaks of the phase-locked regime have disappeared. As  $R$  is increased, the peaks gradually broaden and the gaps between them become shallower, until nearly featureless spectra are produced, as in figure 7(e).

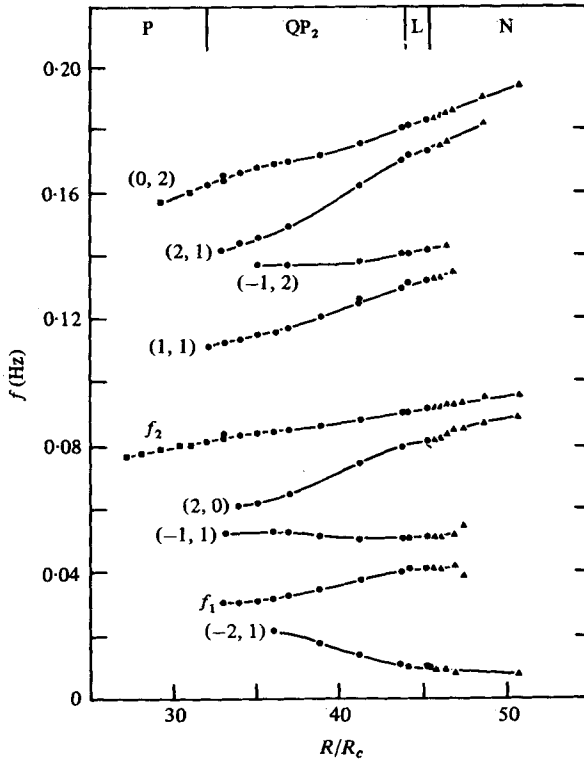


FIGURE 10. Frequencies of all statistically significant spectral peaks as a function of  $R/R_c$  for route I $\alpha$ . The numbers in parentheses identify sums and differences of  $f_1$  and  $f_2$ . Squares, circles and triangles are used in the periodic, quasi-periodic or locked, and non-periodic dynamical regimes, respectively.

In this spectrum, the power falls as  $f^{-4.3 \pm 0.5}$ , in agreement with the observations of Ahlers & Behringer (1979) at larger aspect ratio.

In order to describe the growth of noise quantitatively, we determined the linewidth of spectral peaks as a function of  $R/R_c$  above the onset of noise. As figure 9 demonstrates, the linewidth is approximately linear in  $(R - R_t)/R_c$ , where the extrapolated turbulent threshold  $R_t/R_c$  is about 45, slightly below the value 46.0 where the non-periodicity becomes obvious from examination of a single spectrum. We conclude from figure 9 that the non-periodic motion has a well-defined onset (answering a question posed in the introduction) and that the noise grows smoothly with Rayleigh number above this onset.

The frequencies  $f_1$  and  $f_2$  increase with  $R$ , as shown in figure 10. All of the statistically significant peaks are plotted and labelled with the integers  $(m_1, m_2)$  specifying the linear combinations; for example,  $(-2, 1)$  denotes the peak at  $(-2f_1 + f_2)$ . The symbols in the figure are differentiated to indicate the distinct dynamical regimes P, QP<sub>2</sub> or L, and N. The frequencies in the non-periodic regime are only known to about 1% because of the broadening of spectral features.

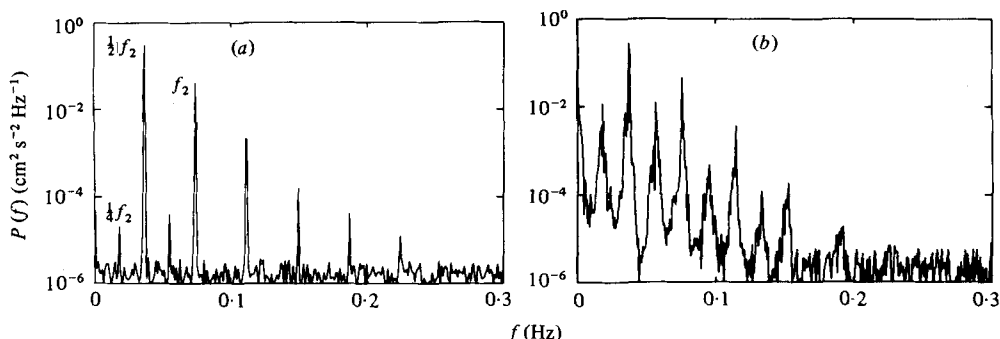


FIGURE 11. (a) Spectrum showing subharmonic (period doubling) bifurcation to frequencies  $\frac{1}{2}f_2$  and  $\frac{1}{4}f_2$  (see discussion of route II),  $R/R_c = 27.0$ . In (b), the motion has just become non-periodic and the peak at  $\frac{1}{4}f_2$  is quite strong,  $R/R_c = 28.0$ .

#### 4.4. Route II: subharmonic (period doubling) bifurcations

Non-periodicity can be obtained after several successive subharmonic bifurcations at  $\Gamma = 3.5$  and  $P = 2.5$ , and perhaps under other conditions as well. A similar process had been seen earlier in mathematical models as simple as mappings of the unit interval of the form  $x_{n+1} = f(x_n)$ .

We observe the following sequence of instabilities leading to turbulence via subharmonic bifurcations. The periodic state has an onset at  $R/R_c = 17$ , substantially lower than that at  $P = 5.0$  described in §4.3. The amplitudes of the peak (again denoted by  $f_2$ ) and its harmonics grow with increasing  $R$ , until a subharmonic bifurcation at  $R/R_c = 21.5$  doubles the period of the oscillation. This instability is indicated by a peak at  $\frac{1}{2}f_2$  (and harmonics) which grows rapidly with  $R$  and eventually dominates  $f_2$ . A second subharmonic bifurcation occurs at  $R/R_c = 26.5$ , and produces peaks at  $\frac{1}{4}f_2$  and harmonics in the spectrum, as shown in figure 11. The peak at  $\frac{1}{4}f_2$  is again very weak at first, but grows quickly and continues to grow even after the onset of non-periodicity at  $R/R_c \cong 28$ . There may also be a small region near  $R/R_c = 28$  where the motion is quasi-periodic ( $\text{QP}_2$ ). The spectrum shows many closely spaced peaks resulting from a slow modulation in the time domain, but the presence of noise cannot be ruled out. Hence the existence of a quasi-periodic regime is uncertain. At  $R/R_c = 29$ , the spectra are clearly broadband, and they are nearly featureless at  $R/R_c = 40$ .

Each of the transitions described in this section has hysteresis of about unity in  $R/R_c$  and average values are quoted above.

#### 4.5. Route III: three frequencies

Quasi-periodic states characterized by three distinct frequencies were found in several cases (see figure 6). We summarize here the evidence obtained at  $\Gamma = 3.5$  and  $P = 5$ . The mean flow in each case is characterized by three rolls, but we do not know if this is significant. The flow becomes periodic at  $R/R_c \cong 30$  with a frequency ( $0.110$  Hz) that is higher than in the previous sections because of the higher wavenumber. Instabilities leading to the second and third frequencies occur at  $R/R_c = 39.5$  and  $41.5$ , and a typical spectrum containing all three is shown in figure 12. Broadband noise begins to grow at  $R/R_c = 43$  and the peaks also become broadened.

In order to verify that three basic frequencies are both necessary and sufficient to

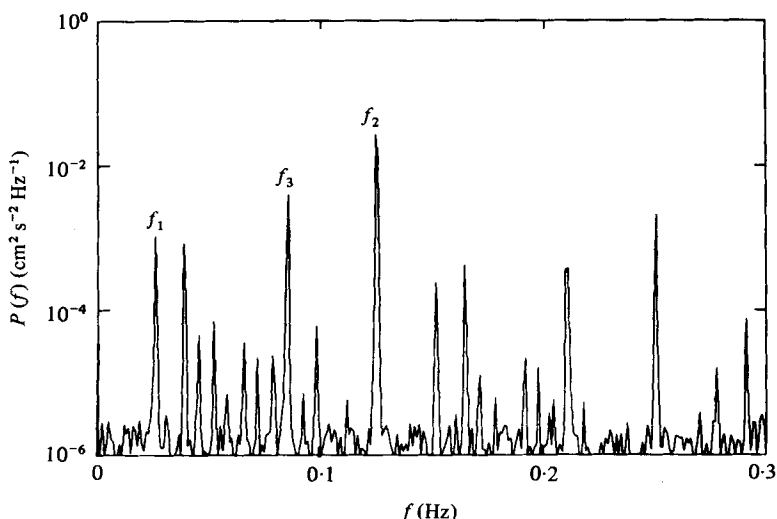


FIGURE 12. Spectrum showing presence of three incommensurate frequencies (route III*d*),  $R/R_c = 42.3$ . All peaks are linear combinations of the three frequencies  $f_1$ ,  $f_2$ , and  $f_3$ .

describe figure 12, we used the following procedure. First, the three highest peaks were selected and their frequencies  $f_1$ ,  $f_2$ , and  $f_3$  were determined by the method of §3.3. Integers  $m_1$ ,  $m_2$ , and  $m_3$  (less than 20) were chosen for each spectral line by matching its frequency to the equation  $F = m_1 f_1 + m_2 f_2 + m_3 f_3$  as closely as possible. Now holding the integers fixed, a least squares fit to all of the lines was performed, with the  $f_i$  as adjustable parameters. This slightly modified the  $f_i$  from the original estimates, and provided an estimate of the goodness of fit by the chi-squared criterion. We found  $\chi^2$  to be 34.5 with 20 degrees of freedom, which is acceptable in view of the limited accuracy with which we know  $\sigma_f$ , the standard error of the measured frequencies. The resulting fit is given in table 1. For each spectral line, the measured frequency  $f$ , its estimated standard error, the fitted frequency  $F$ , and the three integers  $m_i$  are listed.

In order to demonstrate that three frequencies are not only sufficient but also necessary, we followed this fitting procedure with various combinations of two basic frequencies. No value of chi squared less than 1700 could be obtained when the integers were restricted to values less than 20. This clearly rules out the possibility of a satisfactory two-frequency fit to the peaks in figure 12. We also eliminated the possibility of aliasing in the spectrum, and verified that no combination of integer multiples of the  $f_i$  was equal to zero, for integers less than 20. These facts, combined with the observation that the three ratios  $f_2/f_1$ ,  $f_2/f_3$ , and  $f_3/f_1$  vary smoothly with  $R$ , provide strong evidence that the  $f_i$  are in general incommensurate.

A  $QP_3$  regime was also found for  $\Gamma = 2.4$  and  $P = 5$ . The mean flow was similar to figure 4(e) but with signs reversed. In this case we did not attempt to find the onset of time dependence, but the flow is periodic above  $R/R_c = 97$ . There may be a narrow  $QP_2$  regime near  $R/R_c = 109$ , and three frequencies are definitely present in the range  $110 < R/R_c < 117$ . Above this point, the noise grows rapidly and the spectra at  $R/R_c = 120$  are almost featureless. Three frequencies were never observed for the mean flow of figure 4(a) (two rolls).

$f$ (Hz)	$F$ (Hz)	$\sigma_f$ (Hz)	$m_1$	$m_2$	$m_3$
0.026704	0.026693	0.000005	1	0	0
0.039810	0.039817	0.000002	0	1	-1
0.046183	0.046179	0.000017	0	-1	2
0.053409	0.053386	0.000016	2	0	0
0.066547	0.066510	0.000028	1	1	-1
0.072381	0.072427	0.000037	-2	1	0
0.085991	0.085996	0.000002	0	0	1
0.093232	0.093203	0.000037	2	1	-1
0.099121	0.099120	0.000001	-1	1	0
0.112690	0.112689	0.000072	1	0	1
0.125813	0.125813	0.000001	0	1	0
0.152521	0.152506	0.000009	1	1	0
0.165637	0.165630	0.000008	0	2	-1
0.171985	0.171992	0.000047	0	0	2
0.179197	0.179199	0.000006	2	1	0
0.192336	0.192323	0.000026	1	2	-1
0.198224	0.198240	0.000018	-2	2	0
0.205467	0.205447	0.000074	0	3	-2
0.211805	0.211809	0.000007	0	1	1
0.219048	0.219016	0.000060	2	2	-1
0.251626	0.251626	0.000003	0	2	0
0.278288	0.278319	0.000025	1	2	0
0.291445	0.291443	0.000016	0	3	-1

TABLE 1. Least squares fit of the function  $F = m_1 f_1 + m_2 f_2 + m_3 f_3$  to the frequencies  $f$  of the peaks in figure 12. The integers  $m_i$ , and the estimated error  $\sigma_f$ , in  $f$  are also listed.

#### 4.6. Route IV: intermittent noise

A. Libchaber & J. Maurer (1979, private communication) recently observed in liquid helium a type of intermittent noise that is qualitatively different from the non-periodic flows described in earlier sections. We have found that it also occurs at  $P = 5.0$ , in a cell ( $\Gamma = 2.4$ ) of the same proportions as theirs. The stable mean flow above  $R/R_c = 85$  is that of figure 4(e). It becomes quasi-periodic (QP<sub>2</sub>) at  $R/R_c = 95$  (see the bar graph labelled IV d in figure 5), and the second frequency is visible as an extremely slow but regular modulation in the time record of figure 13(a). The spectrum (not shown) has many closely spaced peaks that overlap somewhat. The low frequency increases slowly with increasing  $R$  until intermittent noise appears at  $R/R_c = 102$ . The dynamical behaviour appears to switch at irregular intervals between a non-periodic state and the quasi-periodic state. Examples of this dynamical discontinuity are clearly visible in figure 13(b). As  $R$  is increased, the formerly quasi-periodic regions of the time record become irregular and eventually the entire record appears non-periodic, with a featureless spectrum.

## 5. Discussion

The various sequences of instabilities are all repeatable, but we have discerned no simple rules for predicting which sequence will occur for a given aspect ratio, Prandtl number, and mean flow. However, several generalizations are supported by the evidence. First, quasi-periodicity with more than two frequencies seems to be associated only with rather complex mean flow patterns. Secondly, phase locking occurs at

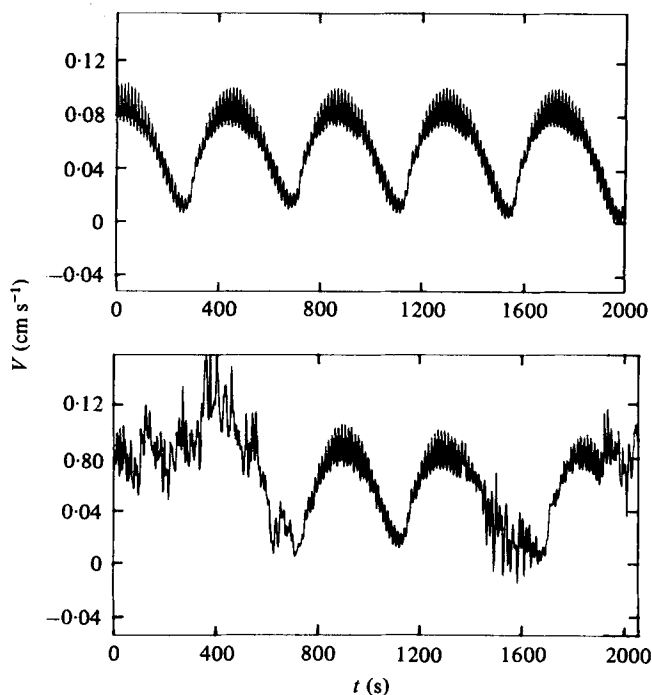


FIGURE 13. Velocity records showing the presence of intermittent noise (route IV). In (a),  $R/R_c = 100.4$ , the fluid is quasi-periodic with frequencies  $f_1 = 0.00233$  and  $f_2 = 0.07563$  Hz. In (b), at  $R/R_c = 102.8$ , intervals of quasi-periodic motion are interspersed between very noisy intervals.

relatively small integer ratios between two characteristic frequencies, and only near the onset of non-periodicity. Thirdly, intermittent noise occurs only for flows that attain rather high Rayleigh number while remaining periodic. Fourthly, quasi-periodicity or subharmonic bifurcation generally precedes non-periodic motion in these experiments.

Not all of our observations fit neatly into the sequences described in §4. For example, the mean flow of figure 4(a) undergoes the sequence  $S \rightarrow P \rightarrow QP_2 \rightarrow S$  at  $\Gamma = 2.4$ . This observation of a reversion to stationary flow at  $R/R_c = 60$  is in striking contrast to the general pattern of increasing complexity of time-dependent motion as the Rayleigh number is increased.

The information contained in figure 6 may be incomplete. For example, it is possible that phase locking occurs more frequently than is noted in the bar graphs, but was missed because of the necessary coarseness of the Rayleigh number scans. Furthermore, some instabilities that do not produce dramatic changes in the spectrum may have entirely escaped detection. We can reliably conclude, however, that some phenomena are pervasive in the transition to turbulent convection at small aspect ratio: quasi-periodicity with as many as three independent frequencies; phase locking; and subharmonic bifurcation.

Because of the large number of parameters needed to characterize the fluid, the geometry, and the boundary conditions, it is difficult to make quantitative comparisons between the observations of different investigators. However, quasi-periodicity

has also been found in circular cells at low aspect ratio by Ahlers & Behringer (1979). Oscillations that may be quasi-periodic have been noted by Olson & Rosenberger (1979). Experiments conducted with cells of larger aspect ratio generally do not show the noise-free quasi-periodic regimes described in this paper (Ahlers 1974; Ahlers & Behringer 1978; Bergé & Dubois 1976; Gollub *et al.* 1977). The transition to turbulent Taylor vortex flow is also characterized by distinct periodic and quasi-periodic regimes (Fenstermacher, Swinney & Gollub 1979). Intermittent noise was first discovered by Libchaber & Maurer (1979, private communication) in rectangular cells of convecting liquid helium ( $P = 1$ ). Libchaber & Maurer (1979) and Maurer & Libchaber (1979) also noted the phenomena of phase locking and subharmonic bifurcation described in §§4.3 and 4.4. Quasi-periodic convection with three incommensurate frequencies has not been reported previously. Finally, the idea that different flow structures can show different routes to turbulence has also been discussed by Bergé (1979).

Quantitative theoretical explanations of the complete sequences of instabilities observed in this work are probably not possible owing to the complexity of the mean flows, the sensitivity to small changes in geometrical parameters and Prandtl number, and the strong nonlinearity of the equations of motion. However, models consisting of a small number of coupled time-dependent amplitudes may be useful even if they do not provide quantitative explanations. Curry's (1978) generalized Lorenz model is particularly interesting in this context because it manifests so many of the phenomena we observe, including subharmonic bifurcation and quasi-periodic motion. It is possible that the lateral boundaries in small aspect ratio experiments restrict the number of modes enough to justify the use of strongly truncated models.

One phenomenon that can probably be successfully explained with simple models is the onset of non-periodicity via phase locking. The entrainment of one oscillator by another is well known in many contexts. One example is the forced Van der Pol oscillator discussed extensively by Flaherty & Hoppensteadt (1978). A system of two coupled tunnel diode relaxation oscillators was also found to exhibit phase locking (Gollub, Brunner & Danly 1978). This simple electronic system has only four dynamical variables, yet it also manifests non-periodic motion. Both the phase locking and the non-periodic motion have been successfully modelled numerically (Gollub, Romer & Socolar 1980). It seems quite likely that the onset of non-periodic convection can also be explained by modelling it as a system of interacting nonlinear oscillators.

The observation of quasi-periodic convection with three generally incommensurate frequencies may have interesting theoretical implications. This motion can be described by a trajectory covering the surface of a three-dimensional torus  $T^3$  in the phase space spanned by the time-dependent Fourier amplitudes of the velocity field (see Fenstermacher, Swinney & Gollub 1979). An interesting theorem about such tori has been proven recently by Newhouse, Ruelle & Takens (1978). It states (paraphrased) that, in every suitably differentiable neighbourhood of a vector field on the torus  $T^m$ , there is a vector field having a non-periodic attractor if  $m \geq 3$ . If this theorem is applicable to the Navier–Stokes equations, it suggests that infinitesimal perturbations of a quasi-periodic motion with three incommensurate frequencies may result in non-periodic motion. Such quasi-periodic motion would then probably not be observable over a significant range in the relevant parameters. The fact that we do observe this behaviour over a finite interval in  $R$  means that the physical relevance of this theorem is as yet obscure. However, the basic prediction of Ruelle & Takens

(1971) that non-periodic motion should occur after a small number of time-dependent instabilities is generally consistent with our observations.

Finally, quantitative predictions for the amplitudes of spectral peaks have been obtained recently (Feigenbaum 1980) for the case of a cascade of subharmonic bifurcations. The theory contains universal scaling parameters and may be applicable to a variety of hydrodynamic problems. A more detailed description of the subharmonic route to turbulence, including maps of the spatial structure of the oscillations and a comparison with the theoretical predictions, appears elsewhere (Gollub, Benson & Steinman 1980).

The diversity of processes involved in the transition to turbulent convection is very great. However, the prevalence of relatively simple phenomena (period doubling bifurcations, quasi-periodic motion, and phase locking) does offer some hope for the possibility of achieving qualitative understanding of the basic processes.

It is a pleasure to acknowledge the contributions of H. Swinney to the planning and execution of this work. We also appreciate extremely helpful discussions with G. Ahlers, P. Hohenberg, D. Joseph, and A. Libchaber. J. Steinman assisted us with recent experiments. This work was supported by the National Science Foundation and the Research Corporation.

#### REFERENCES

- AHLERS, G. 1974 Low-temperature studies of the Rayleigh-Bénard instability and turbulence. *Phys. Rev. Lett.* **33**, 1185.
- AHLERS, G. & BEHRINGER, R. 1978 Evolution of turbulence from the Rayleigh-Bénard instability. *Phys. Rev. Lett.* **40**, 712-716.
- AHLERS, G. & BEHRINGER, R. P. 1979 The Rayleigh-Bénard instability and the evolution of turbulence. *Prog. Theor. Phys. Suppl.* **64**, 186-201.
- BERGÉ, P. 1979 Experiments on hydrodynamic instabilities and the transition to turbulence. In *Dynamical Critical Phenomena and Related Topics* (ed. H. P. Enz). Springer.
- BERGÉ, P. & DUBOIS, M. 1976 Time-dependent velocity in Rayleigh-Bénard convection: a transition to turbulence. *Opt. Comm.* **19**, 129-133.
- BUSSE, F. H. 1978 Non-linear properties of thermal convection. *Rep. Prog. Phys.* **41**, 1929-1967.
- BUSSE, F. H. 1980 Transition to turbulence in Rayleigh-Bénard convection. In *Hydrodynamic Instabilities and the Transition to Turbulence* (ed. H. L. Swinney & J. P. Gollub). Springer.
- BUSSE, F. H. & CLEVER, R. M. 1979. *J. Fluid Mech.* **91**, 319-335.
- BUSSE, F. H. & WHITEHEAD, J. A. 1974 Oscillatory and collective instabilities in large Prandtl number convection. *J. Fluid Mech.* **66**, 67-79.
- CLEVER, R. M. & BUSSE, F. H. 1974 Transition to time-dependent convection. *J. Fluid Mech.* **65**, 625-645.
- CURRY, J. H. 1978 A generalized Lorenz system. *Comm. Math. Phys.* **60**, 193-204.
- DAVIS, S. H. 1967 Convection in a box: linear theory. *J. Fluid Mech.* **30**, 467-478.
- DUBOIS, M. & BERGÉ, P. 1978 Experimental study of the velocity field in Rayleigh-Bénard convection. *J. Fluid Mech.* **85**, 641-653.
- FEIGENBAUM, M. J. 1980 The onset spectrum of turbulence. *Phys. Lett.* **A74**, 375-378.
- FENSTERMACHER, P. R., SWINNEY, H. L., BENSON, S. A. & GOLLUB, J. P. 1979 Bifurcations to periodic, quasiperiodic, and chaotic regimes in rotating and convecting fluids. *Ann. N.Y. Acad. Sci.* **316**, 652-666.
- FENSTERMACHER, P. R., SWINNEY, H. L., & GOLLUB, J. P. 1979 Dynamical instabilities and the transition to chaotic Taylor vortex flow. *J. Fluid Mech.* **94**, 103-128.

- FLAHERTY, J. E. & HOPPENSTEADT, F. C. 1978 Frequency entrainment of a forced Van der Pol oscillator. *Stud. Appl. Math.* **58**, 5–15.
- GOLLUB, J. P. & BENSON, S. V. 1978 Chaotic response to periodic perturbation of a convecting fluid. *Phys. Rev. Lett.* **41**, 948–951.
- GOLLUB, J. P. & BENSON, S. V. 1979 Phase locking in the oscillations leading to turbulence. In *Pattern Formation* (ed. H. Haken), pp. 74–80. Springer.
- GOLLUB, J. P., BENSON, S. V. & STEINMAN, J. 1980 A subharmonic route to turbulent convection. *Ann. N.Y. Acad. Sci.* (to appear).
- GOLLUB, J. P., BRUNNER, T. O., & DANLY, B. G. 1978 Periodicity and chaos in coupled nonlinear oscillators. *Science* **200**, 48–50.
- GOLLUB, J. P., HULBERT, S. L., DOLNY, G. M. & SWINNEY, H. L. 1977 Laser Doppler study of the onset of turbulent convection at low Prandtl number. In *Photon Correlation Spectroscopy and Velocimetry* (ed. H. Z. Cummins & E. R. Pike), pp. 425–439. Plenum.
- GOLLUB, J. P., ROMER, E. J. & SOCOLAR, J. E. 1980 Trajectory divergence for coupled relaxation oscillators: measurements and models. *J. Stat. Phys.* **23**, 321–333.
- KOSCHMIEDER, E. L. 1974 Bénard convection. *Adv. Chem. Phys.* **26**, 177–212.
- KRISHNAMURTI, R. 1970 On the transition to turbulent convection. Part 2. The transition to time-dependent flow. *J. Fluid Mech.* **42**, 309–320.
- KRISHNAMURTI, R. 1973 Some further studies on the transition to turbulent convection. *J. Fluid Mech.* **60**, 285–303.
- LIBCHABER, A. & MAURER, J. 1978 Local probe in a Rayleigh–Bénard experiment in liquid helium. *J. Phys. Lett.* **39**, L369–L372.
- LIBCHABER, A. & MAURER, J. 1979 Une expérience de Rayleigh–Bénard de géométrie réduite: multiplication, accrochage et démultiplication de fréquences. *J. Phys.* (to appear).
- LIPPS, F. B. 1976 Numerical simulation of three-dimensional Bénard convection in air. *J. Fluid Mech.* **75**, 113–148.
- LORENZ, E. N. 1963 Deterministic nonperiodic flow. *J. Atmos. Sci.* **20**, 130–141.
- MAURER, J. & LIBCHABER, A. 1979 Rayleigh–Bénard experiment in liquid helium: frequency locking and the onset of turbulence. *J. Phys. Lett.* **40**, L419–L423.
- MCLAUGHLIN, J. B. & MARTIN, P. C. 1975 Transition to turbulence in a statically stressed fluid system. *Phys. Rev. A* **12**, 186–203.
- MONIN, A. S. 1979 On the nature of turbulence. *Sov. Phys. Usp.* **21**, 429–442.
- NEWHOUSE, S., RUELLE, D. & TAKENS, F. 1978 Occurrence of strange axiom  $A$  attractors near quasi-periodic flows on  $T^m$ ,  $m \geq 3$ . *Comm. Math. Phys.* **64**, 35–40.
- NORMAND, C. Y., POMEAU, Y. & VELARDE, M. G. 1977 Convective instability: a physicist's approach. *Rev. Mod. Phys.* **49**, 581–624.
- OLSON, J. M. & ROSENBERGER, F. 1979 Convective instabilities in a closed vertical cylinder heated from below. Part 1. Mono-component gases. *J. Fluid Mech.* **92**, 609–629.
- OTNES, R. K. & ENOCHSON, L. 1972 *Digital Time Series Analysis*, p. 286. Wiley.
- RUELLE, D. & TAKENS, F. 1971 On the nature of turbulence. *Comm. Math. Phys.* **20**, 167–192.
- SALTZMAN, B. 1962 Finite amplitude free convection as an initial value problem. *J. Atmos. Sci.* **19**, 329–341.
- STORK, K. & MÜLLER, U. 1972 Convection in boxes: experiments. *J. Fluid Mech.* **54**, 599–611.
- WILLIS, G. E. & DEARDORFF, J. W. 1970 The oscillatory motions of Rayleigh convection. *J. Fluid Mech.* **44**, 661–672.